Observation of a temperature dependent asymmetry in the domain structure of a Pd-doped FeRh epilayer

Observation of a temperature dependent asymmetry in the domain structure of a Pd-doped FeRh epilayer

2014 New J. Phys. 16 113073

(http://iopscience.iop.org/1367-2630/16/11/113073)

New Journal of Physics
The open access journal at the forefront of physics
Deutsche Physikalische Gesellschaft DPG | IOP Institute of Physics

Observation of a temperature dependent asymmetry in the domain structure of a Pd-doped FeRh epilayer

C J Kinane[1], M Loving[2], M A de Vries[3,7], R Fan[1,8], T R Charlton[1], J S Claydon[3], D A Arena[4], F Maccherozzi[5], S S Dhesi[5], D Heiman[6], C H Marrows[3], L H Lewis[2] and Sean Langridge[1]

[1] ISIS, Rutherford Appleton Laboratory, Harwell Science and Innovation Campus, Science and Technology Facilities Council, Oxon, OX11 0QX, UK
[2] Department of Chemical Engineering, Northeastern University, Boston, MA 02115, USA
[3] School of Physics and Astronomy, University of Leeds, Leeds LS2 9JT, UK
[4] National Synchrotron Light Source, Brookhaven National Laboratory, Upton, NY 11973-5000, USA
[5] Diamond Light Source Ltd, Harwell Science and Innovation Campus, Didcot, Oxfordshire OX11 0DE, UK
[6] Department of Physics, Northeastern University, Boston, MA 02115, USA
E-mail: christy.kinane@stfc.ac.uk

Received 25 June 2014, revised 9 October 2014
Accepted for publication 14 October 2014
Published 26 November 2014
New Journal of Physics **16** (2014) 113073
doi:10.1088/1367-2630/16/11/113073

Abstract

Using x-ray photoelectron emission microscopy we have observed the coexistence of ferromagnetic and antiferromagnetic phases in a (3 at%)Pd-doped FeRh epilayer. By quantitatively analyzing the resultant images we observe that as the epilayer transforms there is a change in magnetic domain symmetry from predominantly twofold at lower temperatures through to an equally weighted combination of both four and twofold symmetries at higher temperature. It is postulated that the lowered symmetry Ising-like nematic phase resides at the near-surface of the epilayer. This behavior is different to that of undoped FeRh suggesting that the variation in symmetry is driven by the competing structural and electronic interactions in the nanoscale FeRh film coupled with the effect of the chemical doping disorder.

[7] Current address: School of Chemistry, The University of Edinburgh, Edinburgh, EH9 3JJ, UK.
[8] Current address: Diamond Light Source Ltd, Harwell Science and Innovation Campus, Didcot, Oxon, OX11 0DE, UK.

Keywords: FeRh, magnetic thin films, magnetic phase transitions, nucleation, ferromagnetism, antiferromagnetism, domain structures

1. Introduction

The binary alloy FeRh exhibits a fascinating first-order transition from an antiferromagnetic (AFM) to a ferromagnetic (FM) state around 400 K [1, 2]. This transition is accompanied by a significant magnetoresistance [3–6], a large lattice expansion [7, 8] and entropy release [4]. The ability to produce epitaxial thin films of FeRh has revealed additional complexity with a surface related FM state present in the nominally AFM phase [9, 10]. These results have been confirmed by near-surface sensitive real-space imaging performed using soft x-ray photoelectron emission microscopy (XPEEM) which show significantly different behavior for capped and un-capped samples [11, 12]. Temperature-dependent, hard x-ray photoemission spectroscopy has demonstrated changes in the core Fe 2p levels and in the valence band structure in remarkable agreement with results obtained from density functional theory [13, 14] and show that the metamagnetic transition is likely to be driven by an electronic transition. ^{57}Fe conversion electron Mössbauer spectroscopy has also revealed a strain-driven reorientation of the spins at the AFM–FM phase transition in FeRh thin films [15]. Hall-effect measurements across the metamagnetic transition are also consistent with an electronic transition leading to a large increase in the carrier density in the FM phase. This effect has recently been utilized in a room temperature controllable resistor [16] making use of the anisotropic magnetoresistance in the AFM state of the FeRh. Furthermore, FeRh has attracted significant interest due to its ultrafast dynamics in which there is much debate over the out-of-equilibrium state [17–19].

The magnetic behavior of FeRh is strongly affected by doping with other transition metals [20–22]. The AFM to FM transition temperature can be increased by doping with Ir and Pt and decreased by doping with Pd and Ni. This allows the AFM to FM transition temperature to be tuned down to room temperature [23–25]. Doping FeRh with Pd ($FeRh_{1-x}Pd_x$) has been shown, in bulk samples, to preserve the B2 CsCl structure. However, the c/a ratio increases linearly with increased Pd doping [20, 21]. The Pd is known to substitute onto the Rh sites [21] and continues up to the level $x \approx 0.3$ where an AFM-paramagnetic transition replaces the AFM–FM transition. It is also possible to tune the FeRh transition via pressure [26] and magnetic field [27]. In the case of pressure tuning, the transition temperature increases by $\approx 5\,\mathrm{K\,kbar^{-1}}$ [28], while for field tuning it decreases by $\approx 8\,\mathrm{K\,T^{-1}}$. Recently the injection of spin-polarized current [29] has been shown to promote the transition in FeRh from AFM to FM.

As the FeRh transition is thermodynamically first-order there is expected to be a phase coexistence as the system transforms. In thin films the structural phase coexistence is clearly evident from the observation of a well defined change in the out-of-plane lattice parameter and a small change in the in-plane lattice parameters associated with the differing unit cell sizes of the AFM and FM phases [9, 30]. Furthermore, in the transition region there is expected to be a magnetic phase coexistence of AFM and FM regions. This phase coexistence has been observed using x-ray diffraction (XRD) [31] along with a more distinct separation of the phases on cooling through the transition than on warming. This is found to be consistent with a melting/freezing first order phase transition.

The large change in the unit cell volume at the phase transition, a corresponding electronic transition [5, 13, 32] and a change in the sign and magnitude of the magnetic exchange coupling, is a surprisingly high level of complexity for a binary alloy.

In this report, we image the magnetic phase coexistence in a Pd doped FeRh thin film, for a single cooling and warming cycle and observe an unusual Ising-like nematic ordering upon warming into the FM state from the AFM state. A stable and controllable domain structure in the hysteretic regime with electronic and magnetic phase coexistence could be harnessed for novel functionalities [33], for example in memory cells. For such applications it would be highly desirable for the hysteretic regime to be centred around room temperature.

2. Sample preparation and characterization

The sample studied is an epilayer grown by dc magnetron sputtering on MgO single crystal substrates according to the methods described in [34]. In this work we have doped the FeRh with 3 at% Pd which conveniently pushes the transition temperature down close to room temperature [5]. The film was co-deposited from separate angled Fe and Rh sources. Pd doping was provided by a small strip of Pd placed on the surface of the Rh target. The base pressure of the growth system was 5×10^{-8} Torr and the substrate temperature was 600 °C. Ar gas with 4% H_2 at 3 mTorr was used as the sputter gas. The film was post-growth annealed at 700 °C for 60 min, and then cooled to 100 °C before being capped *in situ* with 30 Å of Al. A schematic of the structure is shown in the inset of figure 1(a). The FeRh composition was determined by energy dispersive x-ray (EDX) spectroscopy, on a ≈100 nm lamella prepared using focussed ion beam techniques, as Fe(48 at%)/Rh (49 at%)/Pd(3 at%) with a 3 at% error.

Low-angle x-ray reflectivity (XRR) data shown in figure 1(a) was used to determine the average structure of the epilayer. At low angles the technique is not sensitive to the crystallinity and the electron density depth profile over the whole sample is analyzed using the GenX reflectivity fitting package [35]. The resultant depth profile is shown in figure 1(b). The MgO substrate interface has a root mean squared roughness (rms) of approx 12.5 ± 0.02 Å with the surface/cap region significantly more diffuse. Unsurprisingly the Al cap has oxidized or partially oxidized forming a less dense but thicker oxide layer over a partially oxidized region of Al, as both layers move slightly away from there bulk values. The bulk FeRh(Pd3%) layer was found to be 542.2 ± 0.2 Å thick. An additional FeRh layer with a slightly higher density compared to bulk FeRh with a thickness of ∼35 Å was introduced between the bulk FeRh(Pd) and the Al cap layer in order to fully describe the reflectivity data [12, 36]. This was introduced in so the model could have a density gradient near the surface of the FeRh beyond that descibed by rms roughness parameter alone. The fitting parameters are displayed in table 1. Models with two (nominal structure) or three (Al layer split in two) layers did not give a reasonable fits to the data, failing to reproduce the low **Q** oscillations near the critical edge.

XRD data are shown in figure 2. Clear (001) and (002) diffraction peaks of the highly-chemically-ordered FeRh phase with the B2 CsCl structure (α' phase) are observed. The average out-of-plane lattice constant at room temperature was calculated from the FeRh (00L) peak positions and has a value of 2.998 Å. This value matches the undoped sample c = 2.995 Å and compares favorably to the bulk value of 2.989 Å reported by Lommel [2]. This lattice constant is most certainly not representative of the region near the top of the FeRh(Pd) layer. The widths of the FeRh(Pd) (001) and (002) peaks are the same of those in our undoped

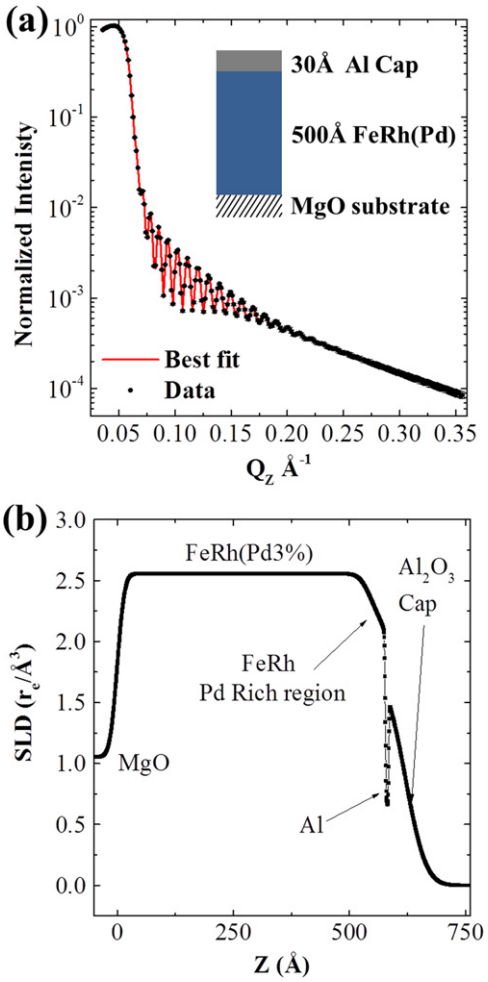

Figure 1. Structural characterization of the FeRh(Pd) epilayer: (a) XRR from the epilayer. The best fit to the data is shown as the solid curve. The inset shows a schematic of the nominal sample stack. (b) The x-ray scattering length density profile extracted from the best fit of the data in panel (a).

Table 1. Table of fitted parameters obtained using the GenX software [35] from the Cu K_αXRR data displayed in figure 1. d is the film thickness, ρ is the layer's scattering length density (SLD) and σ the interfacial rms roughness.

Material	d (Å)	ρ (Atoms Å^{-3})	σ (Å)
Al_2O_3 (cap)	35.5 ± 0.1	0.035 ± 0.001	34.8 ± 0.2
Al(cap)	7.4 ± 0.1	0.067 ± 0.009	1.1 ± 0.2
FeRh(top)	34.9 ± 0.1	0.045 ± 0.007	1.4 ± 0.2
FeRh(Pd 3%)	542.2 ± 0.2	0.036 ± 0.003	17.9 ± 0.7
MgO(sub)	∞	0.052 ± 0.003	12.5 ± 0.02

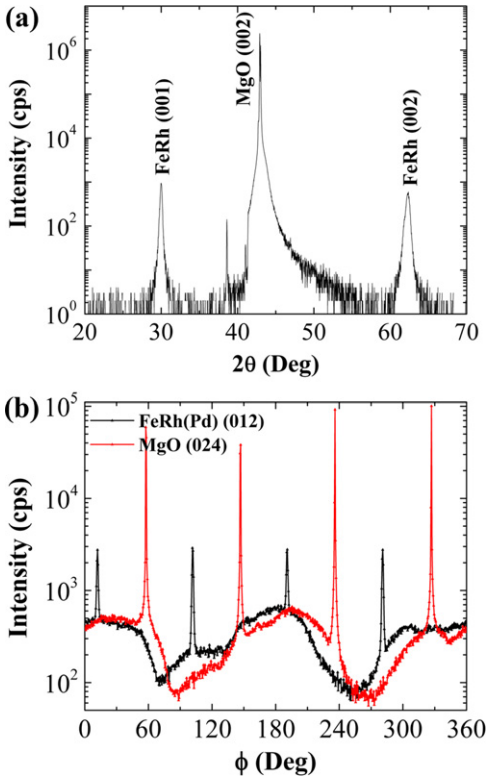

Figure 2. Structural characterization of the FeRh(Pd) epilayer and MgO substrate: (a) high angle Cu K_α XRD of the epilayer showing the highly ordered single crystalline nature of the Pd-doped FeRh film. (b) ϕ-scans through the MgO (024) and FeRh (012) peaks, showing the expected fourfold symmetry.

FeRh samples measured at room temperature. The MgO substrate is known to apply an in-plane compressive strain producing the observed out-of-plane lattice expansion [9]. The long range order parameter **S** was determined using the procedure described by Warren [37]. It was found to be $\mathbf{S} \approx 0.86$ and in good agreement with previous work [32], considering the inclusion of Pd doping. The FeRh(Pd3%) layer was confirmed by XRD to have the expected fourfold in-plane symmetry and the epitaxial relationship to the MgO substrate of FeRh(Pd)[001]‖MgO[001] and FeRh(Pd)[100]‖MgO[110]. The registry of the film and substrate is shown in figure 2(b).

The sample's magnetic properties were studied using SQUID magnetometry and temperature-dependent magnetic force microscopy (MFM) (Bruker MultiMode 8 SPM, employing MESP probes). The field was applied parallel to the edge of the substrate which is along the cubic [001] crystal axis. Figure 3(a) demonstrates that the MgO/FeRh(Pd)/Al film has a bulk-like transition from AFM to FM behavior upon heating to 300 K with a temperature hysteresis of about 30 K. Figure 3(b) shows the sample magnetization M versus applied field H measured at 300 K on warming. The hysteresis loop qualitatively shows coexistence of both ferromagnetism and antiferromagnetism, having a coercive field of ≈80 Oe and a canted hysteresis loop that is not fully saturated at 10 kOe, consistent with the undoped material. Figure 3(c) compares the thermal hysteresis loops of both FeRh(Pd) and pure FeRh measured in an applied field of 50 kOe, so as to shift the transition temperature into the measurement regime of our SQUID magnetometer. Both sample compositions have equivalent saturation moments;

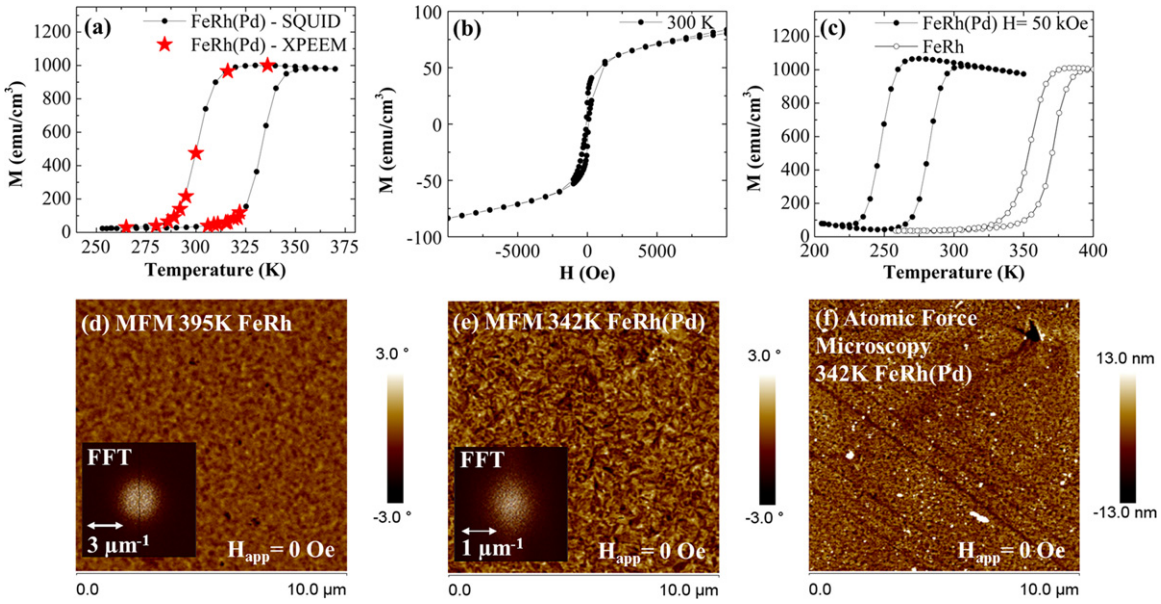

Figure 3. Magnetic characterization of the FeRh(Pd) epilayer: (a) magnetization versus temperature ($M(T)$) measured in a 100 Oe applied field for FeRh(Pd 3%). The red stars correspond to the XPEEM measurement temperatures only. (b) Applied field dependence of the magnetization at 300 K showing a canted hysteresis loop. Panel (c) displays $M(T)$ for both the FeRh(Pd) and FeRh films in a field of 50 kOe to reduce the undoped FeRh transition into the measurable range of the SQUID. Note the similar magnitude of the magnetization and narrowing of the FeRh hysteresis. Panels (d) and (e) show MFM images of the FeRh (395 K) and FeRh(Pd)(342 K) films respectively at a temperature where the films are entering the phase coexistence regime upon warming. The insets in (d) and (e) show the FFTs of the images used to estimate the magnetic domain sizes. The images were measured in zero-field conditions. (f) Atomic force microscopy topographic image of the surface of the FeRh(Pd) sample at 342 K. The diagonal grooves are scratches on the film surface.

the doped system has a wider thermal hysteresis than does the pure system due to the increased disorder derived from the Pd doping.

Panels (d) and (e) of figure 3 show $10\,\mu\text{m} \times 10\,\mu\text{m}$ MFM images of FeRh at 395 K and FeRh(Pd)at 342 K respectively in zero applied magnetic field upon warming. At these temperatures both films are in the process of transforming from the AFM to the FM phase. MFM is inherently sensitive to out-of-plane magnetization, hence in the case of in-plane magnetization it is largely sensitive to domain walls and out-of-plane stray fields. A clear difference is observed between the undoped and doped systems: the undoped FeRh film exhibits isotropic magnetic domains [11] and the Pd-doped FeRh film exhibits smaller, slightly elongated domains. Panel (f) of figure 3 shows the atomic force microscopy topography of the FeRh(Pd) sample imaged at 342 K. The FeRh(Pd) rms surface roughness was found to be 26.5 ± 3.5 Å, via the Gwyddion software package [38]. Large diagonal scratches are visible stretching over the entire map range, however these features are not reproduced in the MFM image. This strongly implies that the surface magnetism is largely decoupled from the surface topography in both films.

The insets show the fast Fourier transforms (FFT) of the MFM images of the FeRh and doped FeRh(Pd) respectively figure 3. To obtain an estimate of the domain size a simple measure was used where the distance at which the FFT intensity had decrease by 1/e from the centre was taken as an indication of the domain size. The cut to which this was applied was always taken in the positive horizontal X direction for consistency. For the FeRh(Pd) the FFT is weakly anisotropic, however the 1/e measure gives a magnetic domain size of approximately 1.4 μm in the horizontal direction. The FFT of the undoped FeRh sample, at an equivalent warming temperature (395 K), gives a larger domain size of 3.8 μm and is isotropic.

3. XPEEM imaging

The in-plane magnetic domain structure of the Pd-doped FeRh film was obtained using x-ray Photoelectron Emission Spectroscopy situated on the Nanoscience Beamline I06 at the Diamond Light Source. In XPEEM measurements the magnetic contrast is obtained through the x-ray magnetic circular dichroism (XMCD) signal. Magnetism and element-specific images were acquired at the Fe L_{III} absorption edge by exciting spin-polarized 2p core electrons into exchange-split unoccupied states above the Fermi level, and imaging the secondary electrons (total electron yield detection) in full-field mode. The beamline optics allow spot sizes of 10 μm to be generated and the final spatial resolution of the microscope is of order 100 nm. The magnitude of the dichroism observed in the XPEEM [39] is proportional to the cosine of the angle between the sample magnetization $\mathbf{M}$ and the direction of the photon helicity $\boldsymbol{\varepsilon}$. Hence XPEEM is sensitive to the magnitude of the vector component of the magnetization (anti) parallel to the direction of the photon propagation and is insensitive to the orthogonal vector components. The XMCD contrast can be extracted as a normalized difference of the observed photon helicity dependent intensities ($I^{\pm}$) defined as the spin asymmetry (SA) $\mathrm{SA} = (I^{+} - I^{-})/(I^{+} + I^{-})$. As a result, the strongest contrast is observed when the magnetization is aligned (anti)parallel to the photon propagation vector.

By acquiring two or more images rotated in this case by 90° or 45° with respect to each other it is possible to produce a vector map of the FM structure. Due to the thin film nature of the system we assume that all the magnetism is in-plane. To maximize the XMCD contrast in the images, the cubic [001] crystal axis of the FeRh(Pd) phase was aligned in the direction of the photon propagation vector. Figure 4(a) shows the vector domain distribution at 342 K upon warming, well inside the FM phase with zero applied magnetic field. As can be clearly seen the sample consists of micron-sized FM domains. An FFT of the vector map (not shown) yields a an average domain size of 1.2 μm in agreement with the MFM image in figure 3(e). The slightly elongated shape of the vector map is due to alignment mismatches between the two images.

From the image we can extract the angular dependence of the magnetization as shown in figure 4(b). This image shows the histogram of all the pixels as a function of angel from 0 to 360°. This displays weak evidence of a magnetocrystalline anisotropy which would reflect the fourfold cubic symmetry of the crystal structure. Recent measurements by Mariager *et al* [40] do not find evidence of strong magnetocrystalline anisotropy in the undoped FeRh.

Figure 4(c) show the modulus of the XMCD SA, giving some indication of the size and strength of the magnetic domains. There are long thin regions with reduced XMCD contrast which can be seen in figure 4(c), localized near the magnetic domain boundaries. At this

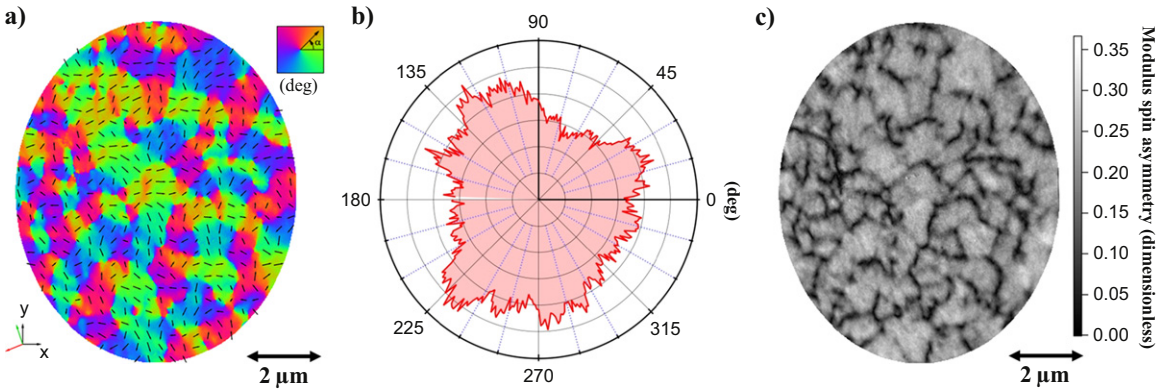

Figure 4. (a) The vector image of the FM domain structure at a sample temperature of 342 K while warming, under zero applied magnetic field. The colour wheel indicates the moment direction. (b) The extracted angular dependence of the magnetization directions. The radial scale is a histogram corresponding to the number of pixels on the vector map as function of angle. (c) Magnitude version of the vector map, obtained by taking the modulus of the XMCD spin asymmetry.

temperature in-plane magnetization is anticipated as we are above the AFM transition, so these are probably domain walls rather than AFM domains.

As was noted in the MFM images, XPEEM domains do not appear to be coupled to structural inhomogeneity in the sample. It was also observed that the domain structure is stable on the time scale of hours at a fixed temperature.

Figure 5 reveals the evolution of the magnetic domain configuration in the FeRh(Pd) sample with temperature as imaged by XPEEM. Starting in the FM phase (figure 5(a)) regions of approximately micron-sized FM domains are visible, with polarization that is both parallel and anti-parallel to the cubic axis. Significant regions are aligned orthogonal to this direction (zero contrast); any AFM regions will also display zero contrast. As the sample is cooled (panels (b)→(d)) the FM domains reduce in size with a concomitant increase in the regions of zero contrast. At 265 K (figure 5(d)) there remains evidence of a weak FM component. The observation of low temperature FM regions in this temperature regime is qualitatively consistent with [9], which proposed a surface arrangement consisting of FM domains in an AFM matrix and with the XPEEM results of Baldasseroni *et al* [11] for an Al-capped FeRh film sample. This result is also corroborated by the observation by Ding *et al* [41] where a small Fe L-edge XMCD signal at room temperature was observed originating in the near surface region of a similar FeRh film.

Warming back through the transition, it is noticeable that the magnetic domain sizes are significantly larger (by a factor of 2) than the size attained through cooling, as shown in figure 5 (e)–(h). Surprisingly, upon warming the domains are elongated along a cubic axis of the epilayer, which are seen at 45° to the horizontal axis. This anisotropy in domain orientation is unusual and unexpected given the fourfold nature of the crystal symmetry.

In the transition region a reduced XMCD contrast is also visible between the domains. These regions are of a congruent shape but smaller size to the high contrast regions. In the case of a strong in-plane cubic anisotropy we would only expect three colour levels on the SA images corresponding to magnetization **M** parallel (red) and antiparallel (blue) to $\boldsymbol{\varepsilon}$ and to orthogonal components or AFM ordering (green). These regions between the (anti-)aligned

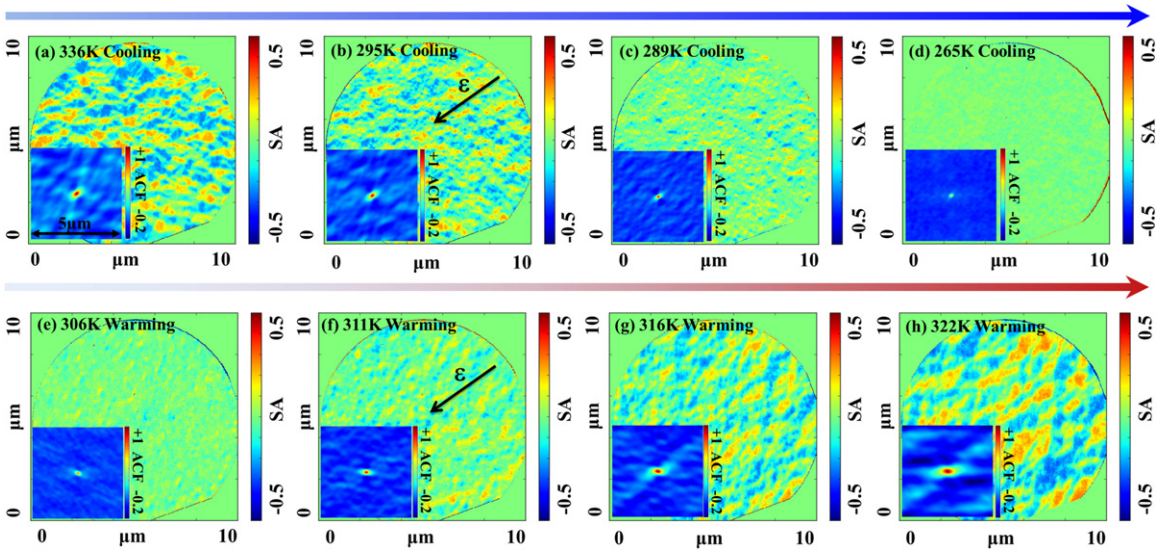

Figure 5. XPEEM images of the magnetic domain evolution of the Pd-doped FeRh film sample taken during progressive cooling, (a) to (d), and warming, (e) to (h), through the FM $\Longrightarrow$ AFM and AFM $\Longrightarrow$ FM transitions respectively. The XPEEM images were taken in zero applied magnetic field. The field of view is 10 μm in diameter. The arrows in panels (b) and (f) represents the photon propagation direction. The colour bar (SA-spin asymmetry) represents the normalized XMCD signal. The insets show 5 μm $\times$ 5 μm ACFs discussed in the text, with 1 and -1 being full correlation and full anti-correlation, respectively, and zero no correlation.

domains presumably primarily contain AFM ordering and domain walls. Finally, after warming above the coexistence regime we recover the fourfold-like structure (figure 4(a)).

4. Analysis and discussion

The XPEEM images allow extraction of the temperature dependence of the magnetization by summing the XMCD contrast within an image, as shown in figure 6(a). We label the mid-point of the AFM–FM transition for the cooling and warming cycles as T_c and T_w respectively. These XPEEM derived results are in good qualitative agreement with the sample-averaged magnetization derived from the SQUID measurements shown in figure 3. There are two main differences, the first is a temperature offset of approximately 7 K between the XPEEM and the SQUID measurements, with the XPEEM data showing the onset of ferromagnetism before that of the SQUID. This might be ascribed to thermometry differences in the two techniques, however it has been shown that a reduced moment but persistent FM region near the cap/film interface approximately 60 Å thick exists as observed in [9]. This region could induce the surface region into a FM state at a lower temperature than the bulk due to the effective exchange field.

Secondly the width of the thermal hysteresis curve measured by the XPEEM technique, around 20 K, is approximately 10 K smaller than those measured by SQUID magnetometry. As the XPEEM technique samples both the surface and near-surface ordering this region dominates the observed signal as compared to the sample bulk averaged SQUID measurements. Fukuda *et al* [42] have demonstrated a Martensitic transition in Pd doped Bulk FeRh, which displays a

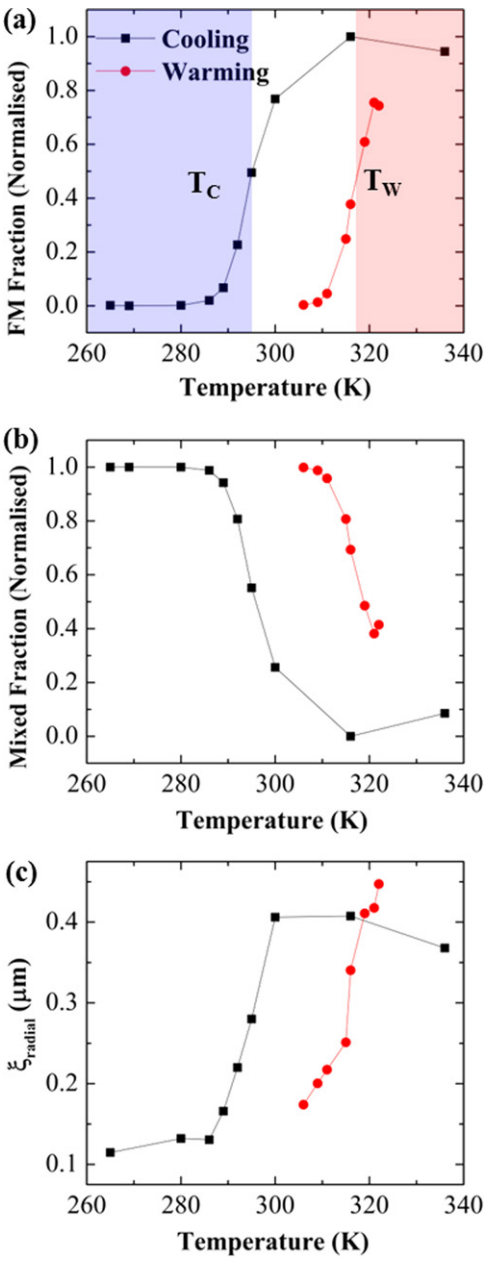

Figure 6. (a) The hysteresis loops extracted from the XPEEM data. The normalized FM magnetization (summation of the SA) as a function of temperature is comparable to that observed by SQUID. The coloured panels represent the regions above and below the midpoint of the transition. (b) The normalized AFM and orthogonal XMCD components (summation of the SA) as a function of temperature. Note the reversal of the hysteresis loop. (c) The correlation lengths ($1/e$) as a function of temperature extracted from the radial intensity plots.

different width of thermal hysteresis loop depending on the warming and cooling history. In our SQUID measurements the cooing arm of the loop was taken to a lower limit of 200 K while the cooling arm of our XPEEM measurements was only taken to 260 K due to time constraints. We suspect that the strain and presence of a surface may drive the surface and near surface region through a martensitic transition which would result in a wider thermal hysteresis compared to the bulk, which is only reset by driving the sample temperature back up above the paramagnetic transition. The bulk FeRh in the work by Fukuda *et al* was doped with 10% Pd while in our case we only have 3% Pd doping, hence it is entirely possible we have not cooled the bulk of the film to a low enough temperature or that there is no transition for 3% Pd doped FeRh in thin film form without strain or a surface to aid in driving the transition.

A sum over the regions of zero XPEEM contrast provides an indication of the degree of AFM phase content as well as regions of orthogonal FM. This is shown in figure 6(b) and we observe an inverted hysteresis loop as expected for the increase and decrease of the AFM phase with cooling and warming respectively.

To quantitatively analyze the phase character of the XPEEM images we have calculated the two-dimensional autocorrelation functions (ACFs) [43] of each real space image, displayed as insets in figure 5. Autocorrelation is a signal analysis tool useful for extracting weak signals in rapidly varying noise, hence its use here in order to quantify domain size and orientation in the XPEEM images. Starting at high temperature (inset figure 5(a)) and cooling, a cross-shaped fourfold symmetric structure is visible with well defined maxima corresponding to a FM domain size of $\approx 1.2\ \mu$m in both the vertical (y) and horizontal (x) directions, indicative of a magnetic domain pattern with that underlying symmetry. As the system is cooled the FM domain signature disappears, and only the central peak is visible (i.e. short range correlations as shown in the inset figure 5(d)) as expected given the loss of XMCD contrast due to the appearance of the AFM phase.

The change in the ACF signal, and hence the magnetic domain behavior on warming the Pd doped FeRh film is more noticeable (inset figure 5(e)). Starting at low temperature the central ACF peak is somewhat elongated. Upon warming into the FM phase the ACF central peak and satellites are anisotropic reflecting the elongation of the FM domain structure, resulting in an Ising-like nematic ordering with a reduced twofold symmetry. This effect is also visible in the real space image of the 322 K Pd doped FeRh film (see figure 5(h)).

As a consistency check, the normalized integrated intensities around concentric circles were calculated as a function of distance from the central point in the image, referred to as a radial intensity plot. Extracting the $1/e$ correlation length of this radial intensity, shown in figure 6(c), recovers the same temperature dependence as that displayed by the magnetization of the Pd doped FeRh film. This method removes any angular dependence on the choice of cut direction, which is necessary since analysis of the diffuse background in 2D ACF images requires further development [43].

To quantify the change in symmetry of the magnetic character of the FeRh(Pd) film in warming and cooling through the first-order phase transition, a circular section through the four ACF satellite peaks as a function of polar angle θ for the 336 and 265 K cooling images are plotted in figures 7(a) and (b). The warming curves are shown on panels (c) and (d). The radius of these circular sections was determined from the ACF for each temperature. The central peak of the ACF is defined as $n = 0$, where n is the order of the peak as a function of increasing radius. The radius of the circular cuts used to generate the angular dependence was chosen to correspond to the nearest neighbor maxima in the ACF, $n = 1$. In order to capture the magnitude

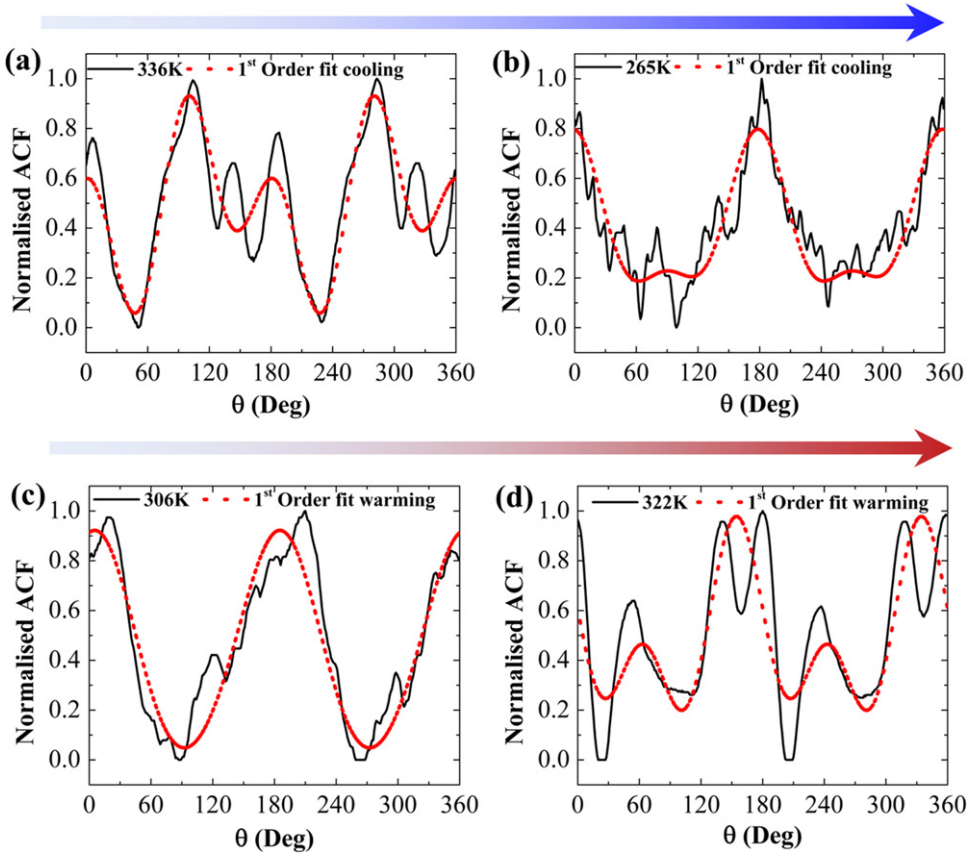

Figure 7. (a) The normalized and smoothed ACF as a function of the polar angle θ at a radius corresponding to the average domain size at 336 K on the cooling branch of the Pd-doped FeRh film. The C_4 symmetry is clearly visible. The dashed curve is the best fit of equation (1). (b) For the lower temperature of 265 K, the ACF is dominated by a twofold C_2 symmetry. Some remanence of the fourfold symmetry is also visible. Panels (c) and (d) show the warming case where the phase with a significant C_2 component moves towards a mixed C_2/C_4 state.

of the different twofold C_2 and fourfold C_4 symmetry terms, we empirically described the circular sections with the following expression:

$$I(\theta) = C_2 \cos^2\left(\theta + \phi_2\right) + C_4 \cos^2\left(2\theta + \phi_4\right), \tag{1}$$

where phase offsets between the twofold and fourfold symmetry terms are given by ϕ_2 and ϕ_4, respectively. Higher order terms in the series were neglected in the fitting. The fits are shown as dotted lines in figure 7.

Figure 8 shows the trend for the C_2 and C_4 components, for the temperatures at which XPEEM imaging was performed for both cooling, figure 8(a) and warming, figure 8(c). In the high temperature region of the cooling panel there is an approximately equal balance of C_4 and C_2 symmetries. Below ≈290 K on cooling and ≈315 K on warming the relative balance changes to become dominated by the C_2 symmetry. From both the SQUID and XPEEM hysteresis loops these temperatures correspond to the mid-point of the transition from AFM ⇒ FM (T_w) and FM ⇒ AFM (T_c).

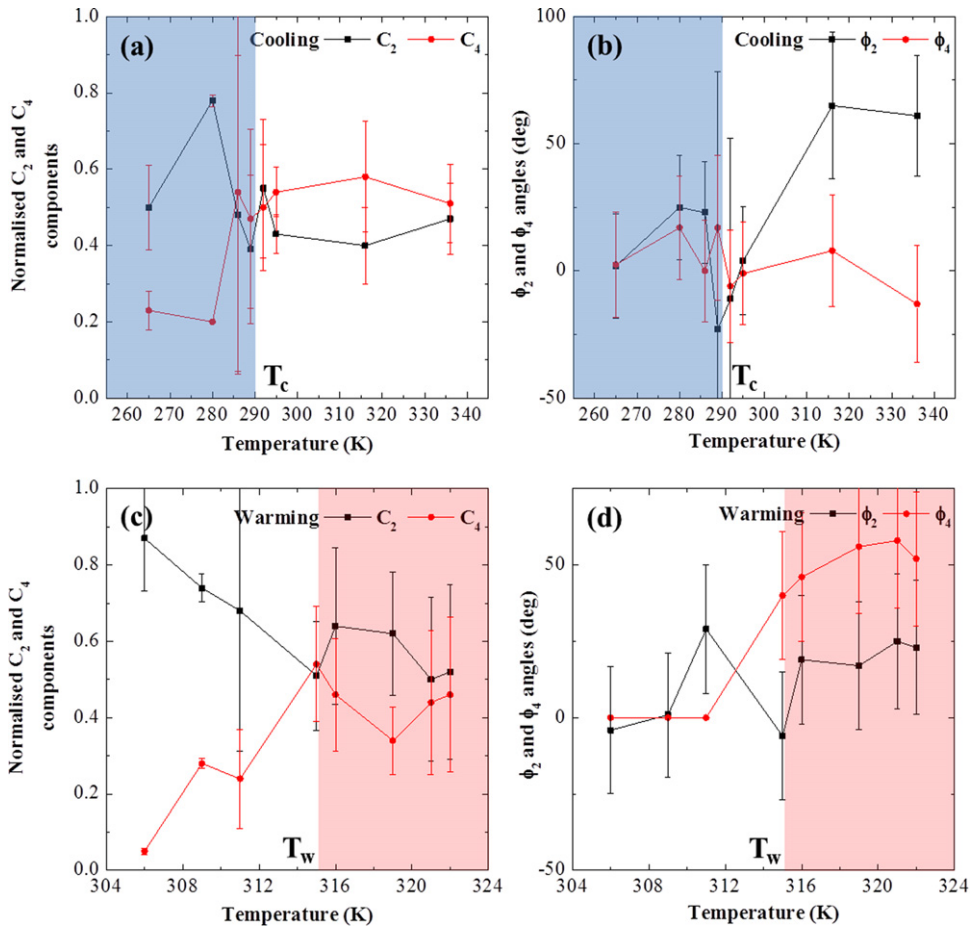

Figure 8. Temperature dependence of the C_4 and C_2 components (a) and (b) obtained from fits to the circular sections of the ACFs for both the cooling and warming cycles and the ϕ_4 and ϕ_2 angle offsets (b) and (d).

Figure 8 panels (b) and (d) show the trend with temperature for the angles ϕ_2 or ϕ_4. In the high temperature region of the cooling panel a rotation of the ϕ_2 angle offset is observed as the system cools through the transition bringing it into coincidence with the ϕ_4 angle. The ϕ_4 angle offset displays almost no change upon cooling. this is consistent with the ϕ_4 component having the four fold symmetry of the crystal and being locked in.

In the warming panel the ϕ_2 curve is essentially flat within error bar and this is attributed to the altered symmetry (two fold surface relief) and magnetization of the surface region due to the martensitic transition. The first three data points for the ϕ_4 curve have arbitrarily been set to zero as as the fit displayed no sensitivity to the ϕ_4 term at these temperatures, due to the C_4 being very small compared to the corresponding C_2 component. However the rest of the ϕ_4 curve is also essentially flat within error bar however is slightly offset by approximately 20°. Given the uncertainties in the PEEM alignment and the subsequent analysis we cannot reliably offer a physical significance to this offset. It should be noted that the parameters were not coupled or correlated in the fitting algorithm and were allowed to vary over there entire ranges.

The origin of the weak magnetic fourfold C_4 symmetry is consistent with the in-plane fourfold crystal symmetry (see figure 2(b)). Conversely, the mechanism leading to the lowered-

symmetry C_2 term is more obscure. In doped FeRh the disorder created by the introduction of Pd into the lattice gives rise to broken translational symmetry, thereby locally modifying the degeneracy of the AFM state and the competing C_4 and C_2 FM ground states. Not only does quenched disorder exist in FeRh(Pd) but a significant elastic strain is present that is generated between the AFM and FM domains arising from the disparity in the AFM/FM unit cell volumes. Clearly, a large elastic strain exists in the undoped material but this does not appear to generate a change in magnetic domain symmetry. Indeed a recent systematic capping layer study [12] appears to downplay the importance of strain in driving the transition. This suggests that the disorder is a significant driver for the observed change in magnetic symmetry. As mentioned earlier in the text, for higher Pd doping ($x \approx 0.1$) it is known that the FeRh(Pd) system adopts a martensite, body centred tetragonal $L1_0$ type order. Such systems exhibit complex shape memory behavior [42] whilst maintaining the AFM–FM transition. We have no evidence of such higher doping levels in our sample from our XRD, EDX result. A detailed analysis of our XRR data does require a graded region at the surface with a slightly higher density than that of the bulk FeRh film. Reference [42] shows that for ($x \approx 0.1$) Pd doped FeRh has two different hysteresis curve widths depending on details of the sample's thermal history. A C_2 symmetry surface relief (stripes) phase was also observed in this work upon cooling, and is characteristic of a martensitic phase. Small regions of the stripe phase persisted up to high temperature and we also see that the ϕ_2 component remains constant upon warming. This would seem a reasonable driving mechanism for the C_2 two fold symmetry component we observe in the XPEEM and its behavior with temperature.

A final observation to be made is that for low temperatures (lower than the mid-point of the two transition temperatures $T \leqslant T_c$, T_w) we recall that a remanent surface FM phase exists in capped epitaxial films. This, coupled with the near-surface sensitivity of the XPEEM technique suggests that the near-surface FM component has a reduced symmetry. The SQUID data in figure 3 when compared to the equivalent XPEEM data in figure 6 implies that the majority of the film is behaving differently. Hence we postulate that the relative influence of the C_2 phase diminishes as the temperature is increased and the bulk of the film transforms into the FM phase. This results in the domain structure reflecting the (weak) bulk-like C_4 symmetry and hence resets the sample.

Having identified the unusual near surface behavior of this doped system it is important that further systematic study is made of the doping and temperature dependence.

5. Summary

To summarize, in a (3 at%)Pd doped FeRh thin film we have observed the coexistence of both AFM and FM order while warming and cooling through the magnetic transition. Quantitative analysis of the in-plane domain structure suggests a temperature-dependent change in symmetry: the expected C_4 symmetry lowers to C_2 in the phase coexistence region and dominates to lower temperature. This behavior is in contrast to that found in the un-doped material. The origins of the different symmetries appear to be linked to the competing disorder present in the system, resulting in a martensitic-like near-surface phase coupled to the more bulk-like ordering within the majority of the epilayer. It is noted that such complexity from a relatively simple alloy is unusual, where even small amounts of doping can dramatically change the nature of the phase coexistence. In this case the interaction of structural, electronic degrees

of freedom and disorder results in a system that can be tuned to operate at room temperature with a stable, and controllable electronic/magnetic domains structure. The complexity of FeRh combined with the fact that it can be controlled via chemical doping leads to interesting functional behavior with possible technological applications.

Acknowledgments

This work was supported by the EPSRC grant reference EP/G065640/1, Department of Energy Office of Basic Energy Sciences and the National Science Foundation (NSF) DMR-0908767 and DMR-0907007. We would like to thank Diamond Light Source Ltd for the provision of x-ray beamtime.

References

[1] Kouvel J S and Hartelius C C 1962 *J. Appl. Phys.* **33** 1343
[2] Lommel J M 1966 *J. Appl. Phys.* **37** 1483
[3] Algarabel P A, Ibarra M R, Marquina C, del Moral A, Galibert J, Iqbal M and Askenazy S 1995 *Appl. Phys. Lett.* **66** 3061
[4] Thiele J-U, Maat S and Fullerton E E 2003 *Appl. Phys. Lett.* **82** 2859
[5] Kushwaha P, Lakhani A, Rawat R and Chaddah P 2009 *Phys. Rev.* B **80** 174413
[6] Suzuki I, Naito T, Itoh M, Sato T and Taniyama T 2011 *J. Appl. Phys.* **109** 07C717
[7] Zsoldos L 1967 *Phys. Status Solidi* b **20** K25
[8] Ibarra M and Algarabel P 1994 *Phys. Rev.* B **50** 4196
[9] Fan R *et al* 2010 *Phys. Rev.* B **82** 184418
[10] Suzuki I, Koike T, Itoh M, Taniyama T and Satora T 2009 *J. Appl. Phys.* **105** 07E501
[11] Baldasseroni C, Bordel C, Gray A X, Kaiser A M, Kronast F, Herrero-Albillos C M, Schneider C, Fadley C S and Hellman F 2012 *Appl. Phys. Lett.* **100** 262401
[12] Baldasseroni C *et al* 2014 *J. Appl. Phys.* **115** 043919
[13] Gray A *et al* 2012 *Phys. Rev. Lett.* **108** 257208
[14] Sandratskii L M and Mavropoulos P 2011 *Phys. Rev.* B **83** 174408
[15] Bordel C, Juraszek J, Cooke D W, Baldasseroni C, Mankovsky S, Minár J, Ebert H, Moyerman S, Fullerton E E and Hellman F 2012 *Phys. Rev. Lett.* **109** 117201
[16] Marti X *et al* 2014 *Nat. Mater.* **13** 367
[17] Quirin F, Vattilana M, Shymanovich U, El-Kamhawy A, Tarasevitch A, Hohlfeld J, von der Linde D and Sokolowski-Tinten K 2012 *Phys. Rev.* B **85** 020103
[18] Thiele J, Buess M and Back C H 2004 *Appl. Phys. Lett.* **85** 2857
[19] Radu I, Stamm C, Pontius N, Kachel T, Ramm P, Thiele J-U, Dürr H A and Back C H 2010 *Phys. Rev.* B **81** 104415
[20] Miyajima H, Yuasa S and Otani Y 1993 *Japan. J. Appl. Phys.* **32** 232
[21] Yuasa S, Miyajima H, Otani Y and Sakuma A 1995 *J. Phys. Soc. Japan* **64** 4906
[22] Yuasa S and Miyajima H 1993 *Nucl. Instrum. Methods* B **76** 71
[23] Baranov N and Barabanova E 1995 *J. Alloys Compd.* **219** 139
[24] Kouvel J S 1966 *J. Appl. Phys.* **37** 1257
[25] Walter P H L 1964 *J. Appl. Phys.* **35** 938
[26] Yuasa S, Miyajima H, Otani Y, Tsuji K, Katayama Y, Kusumi K, Yokoyama H, Yaoita K and Shimomura O 1994 *J. Phys. Soc. Japan* **63** 855
[27] Maat S, Thiele J U and Fullerton E E 2005 *Phys. Rev.* B **72** 214432

[28] Vinokurova L, Vlasov A, Kulikov N and Pardavi-Horvth M 1981 *J. Magn. Magn. Mater.* **25** 201
[29] Naito T, Suzuki I, Itoh M and Taniyama T 2011 *J. Appl. Phys.* **109** 07C911
[30] Kim J W, Ryan P, Ding Y, Lewis L H, Kinane C J, Hickey B J, Marrows C H, Ali M and Arena D A 2009 *Appl. Phys. Lett.* **95** 222515
[31] de Vries M A, Loving M, McLaren M, Brydson R M D, Liu X, Langridge S, Lewis L H and Marrows C H 2014 *Appl. Phys. Lett.* **104** 232407
[32] de Vries M, Loving M, Mihai A P, Lewis L H, Heiman D and Marrows C H 2013 *New J. Phys.* **15** 013008
[33] Cherifi R O *et al* 2014 *Nat. Mater.* **13** 345
[34] Le Graët C, de Vries M A, McLaren M, Brydson R M D, Loving M, Heiman D, Lewis L H and Marrows C H 2013 *J. Vis. Exp.* **80** e50603
[35] Bjorck M and Andersson G 2007 *J. Appl. Crystallogr.* **40** 1174
[36] Loving M, de Vries M a, Jimenez-Villacorta F, le Graët C, Liu X, Fan R, Langridge S, Heiman D, Marrows C H and Lewis L H 2012 *J. Appl. Phys.* **112** 043512
[37] Warren B E 1990 *X-ray Diffraction* (Oxford: Dover Publications)
[38] Nečas D and Klapetek P 2012 *Cent. Eur. J. Phys.* **10** 181
[39] Schneider C M and Schönhense G 2002 *Rep. Prog. Phys.* **65** 1785
[40] Mariager S O, Guyader L L, Buzzi M, Ingold G and Quitmann C 2013 arXiv:1301.4164v1
[41] Ding Y, Arena D A, Dvorak J, Ali M, Kinane C J, Marrows C H, Hickey B J and Lewis L H 2008 *J. Appl. Phys.* **103** 07B515
[42] Fukuda T and Kakeshita T 2013 *J. Alloys Compd.* **563** 192
[43] Sivia D S 2011 *Elementary Scattering Theory: For X-ray and Neutron Users* (Oxford: Oxford University Press)